Steering Electron Density of Zr Sites Using Ligand Effect in Bio-beads for Efficient Defluoridation

Yizhong Zhang, Liuchang Wang, Ruichi Zhang, Chao He, Lixia Jia, Xunliang Wang, Xuemin Feng, Tianxiang Jiang, Baolong Xie, Xiaolei Ma, Junrui Cao, Yuhui Ma, Xin Tan, and Tao Yu**

Y. Zhang, X. Wang, X. Feng, T. Jiang, B. Xie, X. Ma, J. Cao, Y. Ma
Research Team for Environmental Functional Materials, Department of Environmental Technology, The Institute of Seawater Desalination and Multipurpose Utilization, Ministry of Natural Resources (MNR), Tianjin 300192, People's Republic of China
E-mail: mayuhui@isdmu.com.cn

T. Yu
School of Chemical Engineering and Technology, Tianjin University, Tianjin 300350, People's Republic of China
E-mail: yutao@tju.edu.cn

L. Wang
School of Chemical Engineering, Xi'an University, Xi'an 710065, People's Republic of China

L. Jia
School of Environmental Science and Engineering, Tiangong University, Tianjin 300387, People's Republic of China

X. Tan
School of Environmental Science and Engineering, Tianjin University, Tianjin 300350, People's Republic of China

R. Zhang, C. He
Faculty of Engineering and Natural Sciences, Tampere University, Tampere, Finland

Keywords: (fluoride ion, zirconium (hydro)oxides, ligand effect, electronic state modulation, chitosan hydrogel beads)

(Abstract: Because of spontaneous agglomeration effect and undesirable electronic state of Zr sites on the surface, zirconium (hydr)oxides generally exhibit suboptimal defluoridation capacity. Herein, a template confinement-ligand anchoring strategy has been developed by utilizing confined growth of zirconium hydroxide (ZH) inside chitosan hydrogel beads (CHB) and subsequent anchoring of fumaric acid (fm) on its surface Zr sites in a monodentate mononuclear coordination mode. This technique leads to uniform dispersion of ultrafine fmZH (~3.4 nm) and tunable electron density at the Zr sites. Due to the electron-withdrawing ability of fumaric acid, electron delocalized Zr sites increase the orbital energy level matching and vacated *Zr 4d* orbitals to promote hybridization with the *F 2p* orbitals of fluoride ions. Ultimately, robust Zr–F bond can be formed as a result of reduced the adsorption energy towards fluoride ion. In particular, the defluoridation capacity shows positive linear relationship with the electron extraction ability of ligands. The saturation adsorption capacity and dynamic treatment capacity of CHB@fmZH are 10.8 times and 45.9 times higher than that of CHB@ZH, respectively, which was associated with high electron extraction (0.098 e^-) of fm from Zr site. Overall, this work offers a novel insight into the design and synthesis of more high-efficiency metal oxides adsorbents by steering its surface metal sites electronic state through ligand effect.)

1. Introduction

Since Smith[1] and Churchill[2] pointed out in 1931 that the human dental defect disease of mottled enamel was caused by the toxic effect of fluorine in groundwater. As an important indicator of groundwater drinkability, fluorine has gradually received great attention and concern from all over the world.[3] In fact, drinking low concentration of fluorine-containing groundwater is beneficial to human health and can effectively prevent dental caries and osteoporosis, while excessive intake of fluoride can interfere with the enzymes activity and

disrupt the metabolic balance of calcium and phosphorus, and thus leading to dental fluorosis in mild cases and bone and joint deformation in severe cases.[4] Still today, fluoride contamination in groundwater is still a global issue. For example, high concentration of fluoride in groundwater were detected frequently in many countries such as Bangladesh, India, China, the United States, the United Kingdom, South Africa and so on. Therefore, to ensure the safety of drinking water, there is a great need to develop efficient, simple, and cost-effective defluoridation technology.

Adsorption is a classic technique for fluoride removal, which describes the process of fluoride removal by physical or chemical enrichment on the adsorbent surface. As early as 1934, Mckee[5] at Columbia University first reported fluoride removal by adsorption using acid-activated carbon. Various types of adsorbents for fluoride removal have been reported subsequently, such as activated alumina,[6] activated magnesium oxide,[7] zirconium silicate,[8] hydroxyapatite (HAP),[9] iron oxide,[10] zirconium oxide,[11] layered bimetallic hydroxide (LDH),[12] lanthanum oxide,[13] cerium oxide,[14] metal organic framework (MOF),[15] *etc*. Metal oxide adsorbents, especially zirconium (hydro)oxides, are a new generation of highly promising adsorbents for fluoride removal due to their low toxicity, acceptable cost, and chemical stability, but insufficient active Zr site of the bonded surface hydroxyl group (Zr–OH) limits the defluoridation capacity. Catering to the current nanotechnology boom,[16] nano-sized zirconia synthesized using strategies such as morphology control,[11b] component coupling,[11c] and pore confinement[11d] could expose more active sites by increasing specific surface area, which significantly enhance the fluoride removal performance. Nevertheless, the high surface energy on the surface of nanoparticles spontaneously causes agglomerate with each other through van der Waals forces or hydrogen bonding interactions,[17] making it difficult to maintain a good fluoride removal performance. Therefore, it is still challenging to effectively maintain the ultrafine size of the nano adsorbent during the adsorption process.

On the other hand, the interaction or binding strength of the fluoride ion with the active

site on the surface of metal oxide also dominates the fluoride removal capacity. Theoretically, fluoride ion adsorption is achieved by the formation of Zr–F bond through orbital hybridization of *Zr 4d* on surface of zirconium (hydro)oxides with *F 2p* of fluoride ion. Unfortunately, the high electronegativity and the small size of the fluoride ion are not favorable for the orbital hybridization of *F 2p* contributing electrons with the *Zr 4d* empty orbitals, essentially leading to a weak Zr–F bond, thus resulting in a poor fluoride removal performance. Recent studies have attempted to optimize the binding strength to the adsorbate by modulating the electronic state of metal sites. In one study,[18] Co-Fe zeolitic imidazolate frameworks (CFZ) was used for electrocatalytic oxygen reduction reaction (ORR) and oxygen evolution reaction (OER), and the *d* orbital energy level of Co was fine-tuned by electron-withdrawing sulfur groups to optimize the OH* adsorption/desorption free energy (ΔG_{OH*}), resulting in excellent ORR and OER bifunctional activity. Another case[19] demonstrated that P doping into the MoS_2 basal plane decreased the electron density on the S atom, which regulated the energy level matching between the *H 1s* orbital and the *S 3p* orbital to optimize the H adsorption/desorption, thus enhancing the hydrogen evolution reaction (HER) kinetics. Considering these, it is envisioned that modulation of Zr sites electronic state on the surface of zirconium (hydro)oxides may provide a new possibility for efficient removal of fluoride ions.

To achieve the above two goals, we adopted a template confinement-ligand anchoring strategy by growing zirconium hydroxide (ZH) inside chitosan hydrogel beads (CHB) and anchoring fumaric acid (fm) ligand on its surface Zr sites. The confined fmZH maintained an ultrafine size (~ 3.4 nm) to expose more active Zr sites. More importantly, electron delocalization occurred at the Zr sites through metal-to-ligand charge transfer (MLCT) due to electron-withdrawing property of fumaric acid, which promoted better energy level matching between atomic orbitals (*Zr 4d* and *F 2p*) and enabled more *4d* vacant orbitals for hybridization participation, and thus reduced the adsorption energy toward fluorine ions to form robust Zr–F bond. Finally, compared with CHB@ZH without fumaric acid, the saturation adsorption

capacity and dynamic treatment capacity of CHB@fmZH for fluoride ions were increased by 10.8 times and 45.9 times, respectively.

2. Results and Discussion

2.1. Material Synthesis and Structural Analysis

The material preparation process can be described by the **Scheme 1**: the acidity (pH < 1) of zirconium salt solution could realize chitosan dissolution easily at room temperature to obtain a chitosan hydrosol containing Zr^{4+} ions (**Step 1**). This hydrosol was added drop by drop to NaOH solution to form macroscopic scale white beads (**Figure 1a**). During this preparation process, the hydrosol droplets were instantly solidified into hydrogel beads upon contact with NaOH, as the H^+ in the hydrosol was neutralized by adequate OH^-, meanwhile, the Zr^{4+} in the hydrosol momentarily reacted with OH^-, causing confined growth of zirconium hydroxide (ZH) inside chitosan hydrogel beads (CHB) (**Step 2**). Unsaturated Zr sites appeared on the surface of ZH because it tended to form clusters under room temperature and atmospheric pressure, which subsequently anchored carboxylate ions in the fumarate solution to the unsaturated Zr sites by forming Zr–O bonds to obtain fumaric acid-anchored zirconium hydroxide confined inside chitosan hydrogel beads (CHB@fmZH) ultimately (**Step 3**).

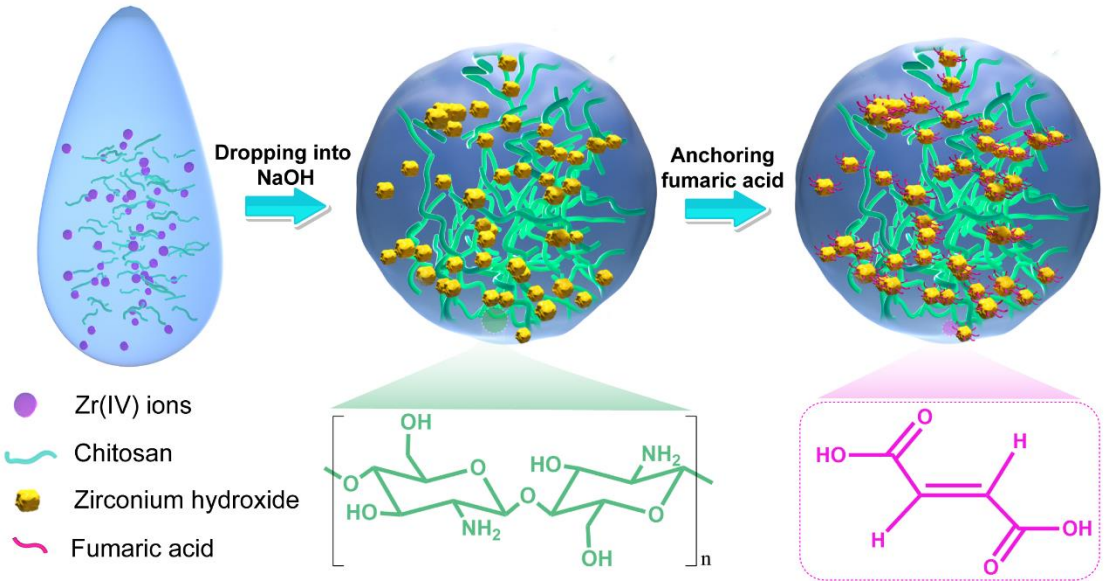

Scheme 1. Schematic illustration displaying the fabrication strategy of CHB@fmZH.

In order to reveal the structural information of the materials, a series of characterizations were performed. According to the scanning electron microscopy (SEM) images shown in **Figure 1b**, there were an abundance of micron- and nano-scale interconnected porous channels on the surface of CHB@fmZH, which could also be confirmed by the results of two double peaks (43.3 μm and 163.6 nm) that appeared in the pore size distribution by mercury intrusion porosimetry (**Figure S1, Supporting Information**). This multi-scale pore structure was conducive to the enhancement of mass transfer at the solid-liquid interface so that fluoride ions might easily draw near surface active sites to complete the adsorption. Some small black spots for ZH particles confined in the chitosan skeleton could be observed in high-resolution transmission electron microscopy (HRTEM) (**Figure 1c**), and its particle size was 3.43 ± 0.03 nm obtained by statistical analysis of the particle size of 50 particles (**Figure 1d**). Therefore, we used the template confinement effect of chitosan to generate of ultrafine fmZH, which was even smaller than previous zirconium (hydr)oxides obtained by gel-type anion exchanger[20] and amyloid fibril carrier.[11c] This was attributed to the unique template effect of chitosan, which exerted growth restriction on crystal nucleus by its skeleton and dispersion on seed crystal by its hydrophilic functional groups ($–NH_2$ and –OH), thus promoting the formation of ultrafine fmZH.

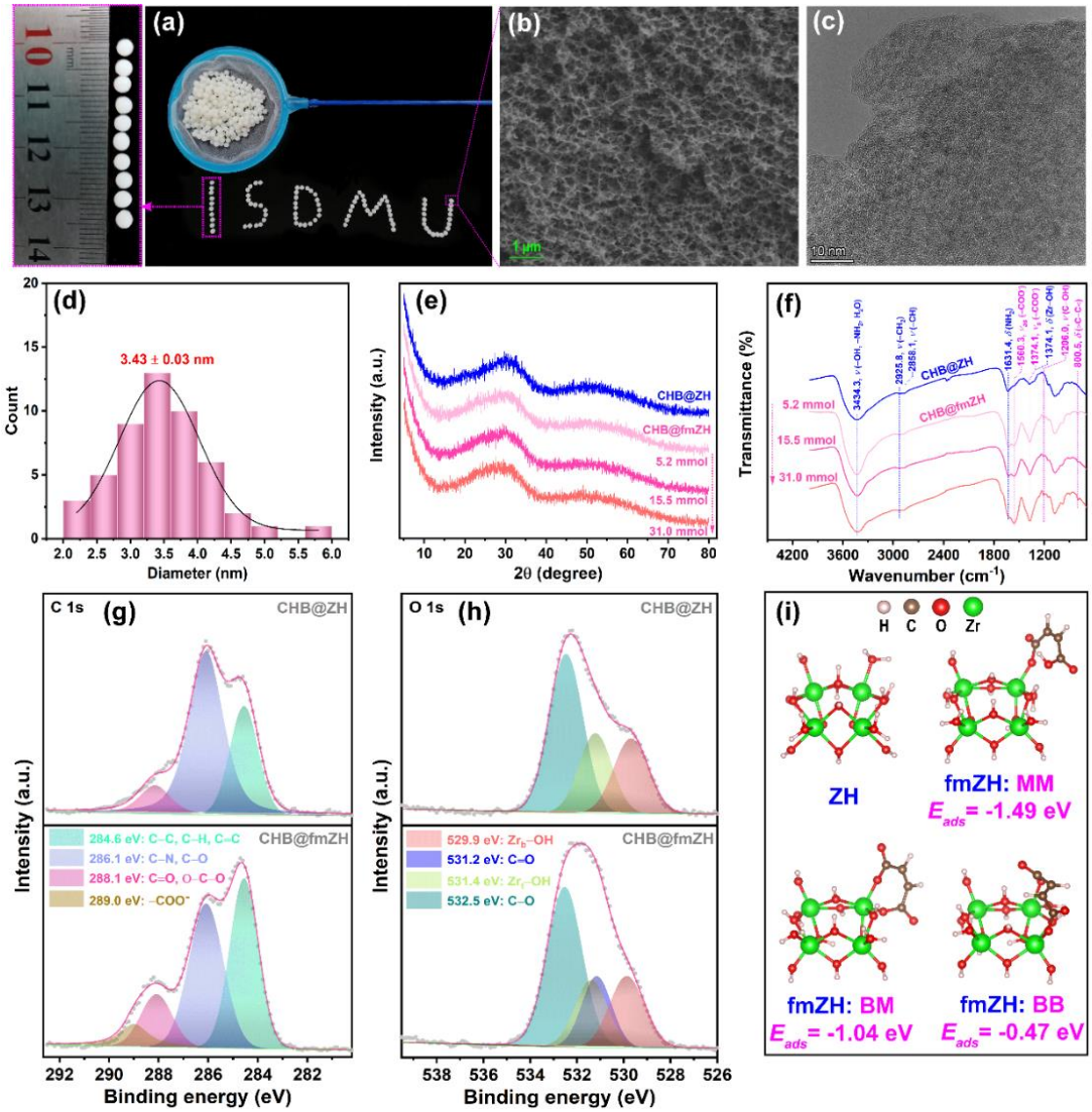

Figure 1. (**a**) Photograph of CHB@fmZH, (**b**) SEM image of CHB@fmZH, (**c**) TEM image of CHB@fmZH, (**d**) histogram of particle size distribution of CHB@fmZH, (**e**) XRD patterns of CHB@ZH and CHB@fmZH, (**f**) FTIR spectra of CHB@ZH and CHB@fmZH, (**g**) C 1s and (**h**) O 1s XPS spectra of CHB@ZH and CHB@fmZH, (**i**) coordination modes of fumaric acid on ZH and the corresponding adsorption energies (E_{ads}) obtained by DFT calculations.

High-angle annular darkfield-scanning transmission electron microscopy (HAADF-STEM) coupled with X-ray energy dispersive spectroscopy (EDS) images from the elements C, N, O and Zr demonstrated that fmZH was uniformly distributed on the chitosan (**Figure S2, Supporting Information**). The XRD patterns of CHB@ZH were very similar to pure ZH (**Figure S3 in Supporting Information**, **Figure 1e**), did not show sharp diffraction peaks and the diffraction peaks were significantly broadened than previously reported cubic or tetragonal zirconia,[21] indicating that the ZH in CHB@ZH displayed poor crystallinity with an amorphous

structure.[21a, 22] In addition, the diffraction patterns of CHB@fmZH anchored with different contents of fumaric acid did not change significantly, indicating that the fumaric acid was only anchored on the surface of ZH and did not change the crystal structure of ZH. Fourier transform infrared spectroscopy (FTIR) was used to further reveal the surface functional groups. CHB@ZH showed both Zr–OH and chitosan-related functional groups (including amino, hydroxyl, methylene, and pyranose rings) (**Figure S4 in Supporting Information**, **Figure 1f**), confirming the coexistence of chitosan and zirconium hydroxide in CHB@ZH. For CHB@fmZH, the emergence of new bands associated with $–COO^–$, C–OH, and C=C groups indicated that fumaric acid was present in CHB@fmZH.[23] The intensity of the vibrational peaks associated with fumaric acid increased with the content of fumaric acid, signifying that the amount of fumaric acid anchored on CHB@fmZH can be readily adjusted. The presence of fumaric acid in CHB@fmZH could also be confirmed by the characterization analysis of C 1s and O 1s XPS spectra. For the C 1s XPS spectra of CHB@ZH (**Figure 1g**), the functional groups of chitosan were observed at the binding energies of 284.6 eV (C–C, C–H, or C=C), 286.1 eV (C–N or C–O), and 288.1 eV (C=O or O–C–O).[24] The newly emerged $–COO^–$ at the binding energy of 289.0 eV together with the increase of the peak area of corresponding C=O or O–C–O[24b, 25] indicated that the fumaric acid was successfully anchored on the surface of CHB@fmZH. For the O 1s XPS spectra, we first identified the terminal hydroxyl group (Zr_t–OH) and the bridging hydroxyl group (Zr_b–OH) in ZH by deconvoluting the O 1s XPS spectra (**Figure S5, Supporting Information**),[26] where the peak area ratio of Zr_t–OH to Zr_b–OH was 1:1 and the binding energy difference was 1.5 eV. Then the O 1s XPS spectra of CHB@ZH were processed with this fitting parameter to obtain three fitted peaks: C–O originating from the chitosan, and Zr_t–OH, Zr_b–OH from the ZH (**Figure 1h**).[26] Further analysis for CHB@fmZH, a new peak corresponding to C=O at the binding energy of 531.2 eV proved the presence of fumaric acid once again.[25, 27]

To investigate the coordination modes of fumaric acid on the surface of ZH in

CHB@fmZH, we used the ZH cluster structure as a model and performed theoretical calculations of the adsorption energy (E_{ads}) under different coordination modes based on density functional theory (DFT, **Text S4** in **Supporting Information**). Fumaric acid contains two carboxyl groups, and its coordination modes to the Zr site on the surface of ZH mainly include monodentate mononuclear (MM), bidentate mononuclear (BM), and bidentate binuclear (BB) coordination. The calculated adsorption energies were −1.49, −1.04 and −0.47 eV, respectively (**Figure 1i**), therefore fumaric acid anchored to the Zr sites on the surface of ZH was the thermodynamically most stable MM coordination mode.

2.2. Fluoride Ion Removal Study

The CHB, CHB@fm, and CHB@ZH exhibited low fluoride removal performance (< 6 mg/g), while the defluoridation capacity was significantly increased to 31.3 mg/g for CHB@fmZH with anchoring fumaric acid (**Figure 2a**). The content of fumaric acid in the preparation process was further optimized, as shown in the inset in **Figure 2a**, the optimal fumaric acid content was 31 mmol. The adsorption isotherms of CHB@fmZH at content gradient of fumaric acid were further obtained (**Figure S6, Supporting Information**), and the adsorption isotherms were all better described by the Langmuir model with a saturation adsorption capacity of 63.98 mg/g under optimal condition (31 mmol fumaric acid), which was as much as 10.8 times better than CHB@ZH (5.90 mg/g, **Figure S6, Supporting Information**). Considering that the confined template of CHB has negligible fluorine ion removal performance (~ 2.10 mg/g) under neutral conditions (**Figure S6, Supporting Information**), we calculated the adsorption capacity of the effective component fmZH to be 88.98 mg/g, which was better than the most metal sites (e.g., Zr, Al, Mg, Ca, Fe, La, Ce, Ti sites) and non-metal sites (N, O sites) based adsorbents reported in the previous literatures (**Table S2, Supporting Information**). In order to exclude the contribution of specific surface area to fluoride ion removal, BET specific surface area values of 26.77 and 38.09 cm^2/g were obtained for CHB@ZH and CHB@fmZH, respectively, according to its N_2 adsorption-desorption isotherms

(**Figure S7, Supporting Information**). CHB@fmZH showed a higher BET surface area than CHB@ZH, which was due to fact that fmZH nanoparticles in fumaric acid-anchored CHB@fmZH were more dispersible, resulting in the formation of smaller nanoparticles (**Figure S8, Supporting Information**). The fluoride removal capacity of CHB@fmZH (1.68 mg/cm^2) was still 7.6 times higher than that of CHB@ZH (0.22 mg/cm^2) after normalization, indicating that anchoring fumaric acid on the surface of ZH in CHB@fmZH was only contributor that intensified the defluoridation ability. In addition, the variation of different residual fluoride ion concentrations over time during adsorption showed that equilibrium reached after 24 h (**Figure 2b**).

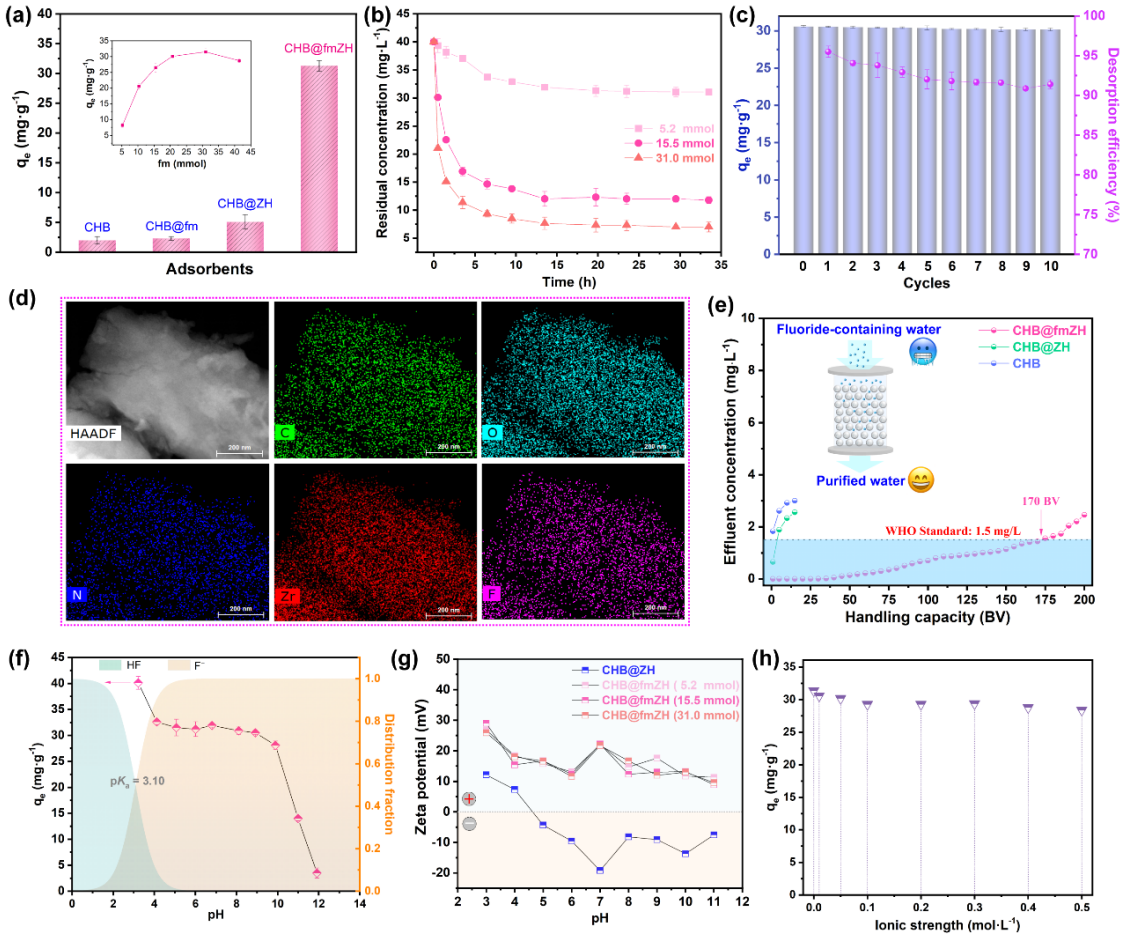

Figure 2. (**a**) Defluoridation capacity of CHB, CHB@fm, CHB@ZH, and CHB@fmZH (the inset for the optimization of fumaric acid content), (**b**) the concentration variation of different residual fluoride ions over adsorption time, (**c**) desorption efficiency and recyclability of CHB@fmZH, (**d**) HAADF-STEM-EDS image of CHB@fmZH after the adsorption of fluoride ions, (**e**) dynamic fixed-bed column experiments for fluoride ions removal, (**f**) fluoride species and removal at different pHs, (**g**) surface zeta potential under different pHs, (**h**) effect of ionic strength on fluoride ion removal.

Reusability is a key issue for the practical application. Desorption efficiency of CHB@fmZH basically stabilized above 90% during the 10 cycles of fluoride ion removal, which provided the premise for excellent recyclability (**Figure 2c**). The adsorbed fluoride ions were uniformly distributed on the surface of CHB@fmZH according to the HAADF-STEM-EDS image after the adsorption of fluoride ions (**Figure 2d**). Moreover, ultra performance liquid chromatography (UPLC) was used to determine fumarate content during the defluoridation process and the IR spectra of CHB@fmZH after adsorption of fluoride ion with different initial concentration was analyzed (**Figure S9, Supporting Information**), we did not detect a large amount of fumarate in the solution, and functional groups associated with fumaric acid still existed in the CHB@fmZH after adsorption, which provided solid evidence to exclude the ion exchange process between fluoride ion and fumarate on the surface. The competitive anions interference test showed that the CHB@fmZH still showed well fluoride removal ability in the presence of common Cl^-, NO_3^-, SO_4^{2-} ions and moderate HCO_3^- and $H_2PO_4^-$ ions in water (**Figure S10, Supporting Information**). To evaluate the application prospect of CHB@fmZH for fluoride removal in groundwater, we performed fixe-bed experiments using synthetic fluoride bearing groundwater. As shown in **Figure 2e**, CHB@fmZH successfully purified 170 BV of effluent to meet the World Health Organization (WHO) standard for domestic drinking water (i.e., $[F]_0 < 1.5$ mg/L), which was 45.9 times as much as CHB@ZH. Furthermore, for a batch adsorption with a higher concentration of fluoride ions (40 mg/L), when the dose of CHB@fmZH (wet state) was higher than 7.5 g/L, it could also result in residual fluoride ion concentration below the WHO standard (**Figure S11, Supporting Information**). And, CHB@fmZH exhibited a wide pH applicability range from 4 to 10 (**Figure 2f**), this may be due to the buffering effect of the conjugate acid-base pair of the anchored fumaric acid-fumarate on the pH of the solution.

2.3. Mechanism of Enhanced Defluoridation by Electron-Withdrawing at Zr Sites

Surface zeta potential of CHB@ZH and CHB@fmZH at different pH was shown in **Fig.**

2g. For CHB@ZH, the surface was positively charged when pH < 4.63 and negatively charged when pH ≥ 4.63. Interestingly, the fumaric acid-anchored CHB@fmZH was positively charged across the tested pH range, which may be attributed to the fact that anchoring fumaric acid on the surface of CHB@fmZH altered its structure of the double-electric layer. In order to verify whether electrostatic interactions dominate the adsorption process, ion strength experiments were performed and the result was shown in **Figure 2h**. The adsorption of fluoride ions by CHB@fmZH remained basically stable as the background NaCl concentration gradually increased to 0.5 mol/L, indicating that electrostatic attraction was not the dominant mechanism for fluoride ion removal although the electrostatic attraction between fluoride ions and positive surface of CHB@fmZH. In fact, electrostatic attraction only provided an important driving force for the rapid approach of fluoride ions to the surface of CHB@fmZH, especially for acidic conditions, which well revealed the existence of specific coordination interactions between the fluoride ions and the Zr sites on the surface of CHB@fmZH.

We used DFT to calculate the electrostatic potential (ESP) distribution on the surface of ZH and fmZH, as shown in **Fig. 3a**, the region with positive electrostatic potential was mainly distributed on the Zr–OH from ZH, while ESP of Zr–OH on the surface of fmZH changed significantly after anchoring fumaric acid on the Zr site of ZH (**Figure 3b**), and the area around C=O on anchored fumaric acid showed a negative electrostatic region, while the larger area around –CH=CH– was positive probably because of the different electron donor and acceptor properties of these groups. Fumarate electron acceptor action, namely the ability to withdraw electrons, plays an important role in enhancing fluoride adsorption, which will be discussed in detail below.

Further, we calculated the adsorption energies of fluoride ions toward different Zr sites on ZH and fmZH based on DFT (**Figure 3d**). For the convenience of presentation, the Zr site of ZH was denoted as Zr–OH, the native Zr site bonded to fumaric acid on fmZH was denoted as $fmZr_1$–OH, and the neighboring and opposite Zr sites not bonded to fumaric acid are denoted

as $fmZr_2$–OH and $fmZr_3$–OH, respectively. The adsorption energies of $fmZr_1$–OH (−2.63 eV), $fmZr_2$–OH (−2.36 eV), and $fmZr_3$–OH (−2.35 eV) were more negative than that of Zr–OH (−2.16 eV), indicating that the adsorption of fluoride ions at Zr site anchored fumaric acid proceeded more favorably thermodynamically. **Figure 3e** shows the projected density of states (PDOS) of *Zr 4d* and *F 2p* on the surface of ZH and fmZH after adsorption of fluorine ions. The overlapping bands of *Zr 4d* and *F 2p* were in the range of −6.08 to 0.405 eV for ZH, while shifted to a lower energy ranged from −6.84 to 0.163 eV for fmZH, demonstrating that more stable Zr–F bond was formed on Zr sites of the fmZH.

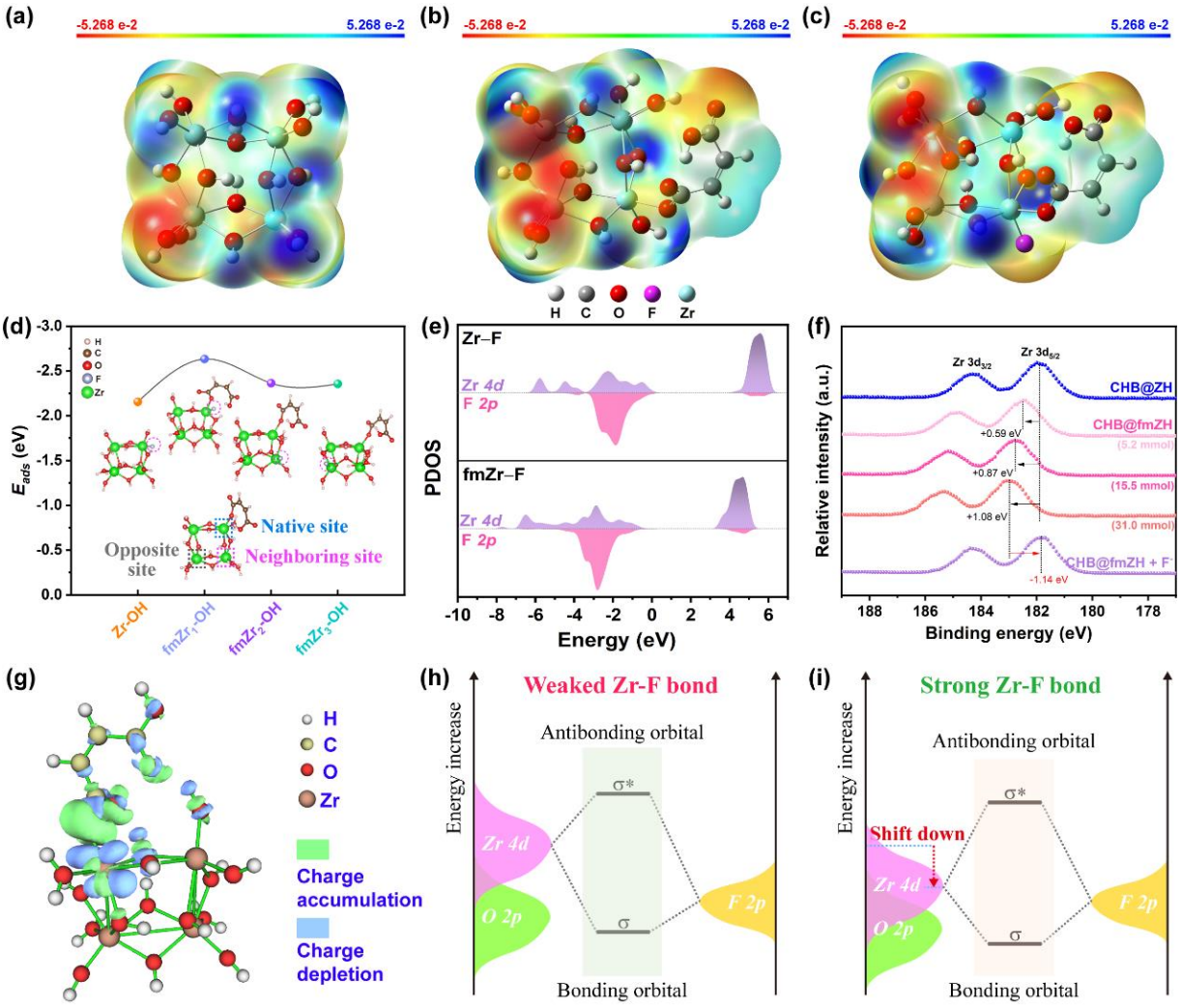

Figure 3. Electrostatic potential of (**a**) ZH, (**b**) fmZH, and (**c**) fmZH–F, (**d**) adsorption energies of fluoride ions toward different Zr sites of ZH and fmZH, (**e**) projected density of states (PDOS) of *Zr 4d* and *F 2p* in the Zr−F for the adsorption of fluoride ions on ZH and fmZH, (**f**) Zr 3d XPS spectra of CHB@ZH, CHB@fmZH, and CHB@fmZH + F^-, (**g**) differential charge density for fmZH; molecular orbital interaction diagram of fluoride adsorption on the surface of (**h**) ZH and (**i**) fmZH.

The chemical environment around the Zr site after fumaric acid anchoring can be identified by the Zr 3d XPS spectra. As shown in **Figure 3f**, binding energies of the Zr $3d_{3/2}$ and Zr $3d_{5/2}$ of CHB@ZH were 184.3 eV and 181.9 eV, respectively. However, the binding energy of CHB@fmZH shifted toward a higher direction and magnitude of the shift was proportional to the amount of fumaric acid, which implied that the electron cloud density around the Zr site decreased after fumaric acid anchoring[28]. The differential charge density for fmZH obtained by DFT calculation was convenient to visualize the electron cloud density variation of Zr site (**Figure 3g**). The bonding region between fumaric acid and Zr site on fmZH can be observed as a charge depletion region around Zr, while the fumaric acid side was a charge accumulation region, indicating that the electrons on Zr site were transferred to fumaric acid. This well corroborated the above XPS analysis results of reduced electron cloud density of Zr site. Therefore, fumaric acid plays a crucial role in steering the electron density at the Zr site on the surface of fmZH. The reduced the electron cloud density on the Zr site by electron-withdrawing fumaric acid could generate electron delocalized *Zr 4d* empty orbital for the filling of electrons from the *F 2p* orbital of the adsorbed fluoride ion to form stable Zr–F bond by orbital hybridization, thus achieving efficient removal of fluoride ions. In addition, according to molecular orbital theory, the participating atomic orbital energy levels should satisfy the principle of similarity when forming molecular orbitals, which determines the formation efficiency of bonding orbitals. The fumaric acid anchored Zr site causes the *Zr 4d* orbital energy level to shift down due to the decrease of electron density (**Figure 3h** and **Figure 3i**), which rendered the *Zr 4d* and *F 2p* orbital energy levels better match and thus effectively promoting the formation of bonding orbitals to generate robust Zr–F.

2.4. The Relationship Between Electron-Withdrawing Ability of Ligands and Defluoridation Capacity

Therefore, it is clear from the above analysis that the ability of fumaric acid to withdraw electrons from Zr sites was the key to the improvement of the fluoride removal performance of

fmZH. To quantify the ability of fumaric acid to extract electrons from Zr sites on fmZH, we deduced the quantity of electrons transferred from Zr sites to fumaric acid to be 0.098 e^- based on the Bader charge analysis obtained from DFT calculations (**Figure 4a**). We further evaluated the electron extraction ability of other organic ligands, including oxalic acid (*ox*), citric acid (*cr*), malic acid (*ma*), propanedioic acid (*pr*) and acrylamide (*am*) (**Figure 4a**, **Text S5** in **Supporting Information**). Ligands, including *ox*, *cr*, *ma* and *pr*, showed the ability to extract electrons from the Zr site, and transferred electrons were 0.083, 0.043, 0.070 and 0.056 e^-, respectively, while the ability to supply electrons was observed on *am* that reverse transferred 0.287 e^- to the Zr site. Defluoridation capacity of ZH anchored by these ligands was shown in **Figure 4b**, compared to pure ZH, the enhanced defluoridation by fmZH, oxZH, crZH, maZH and prZH were observed except for amZH, and fmZH represented the highest fluoride removal capacity, which was attributed to the stronger electron extraction ability of fumaric acid.

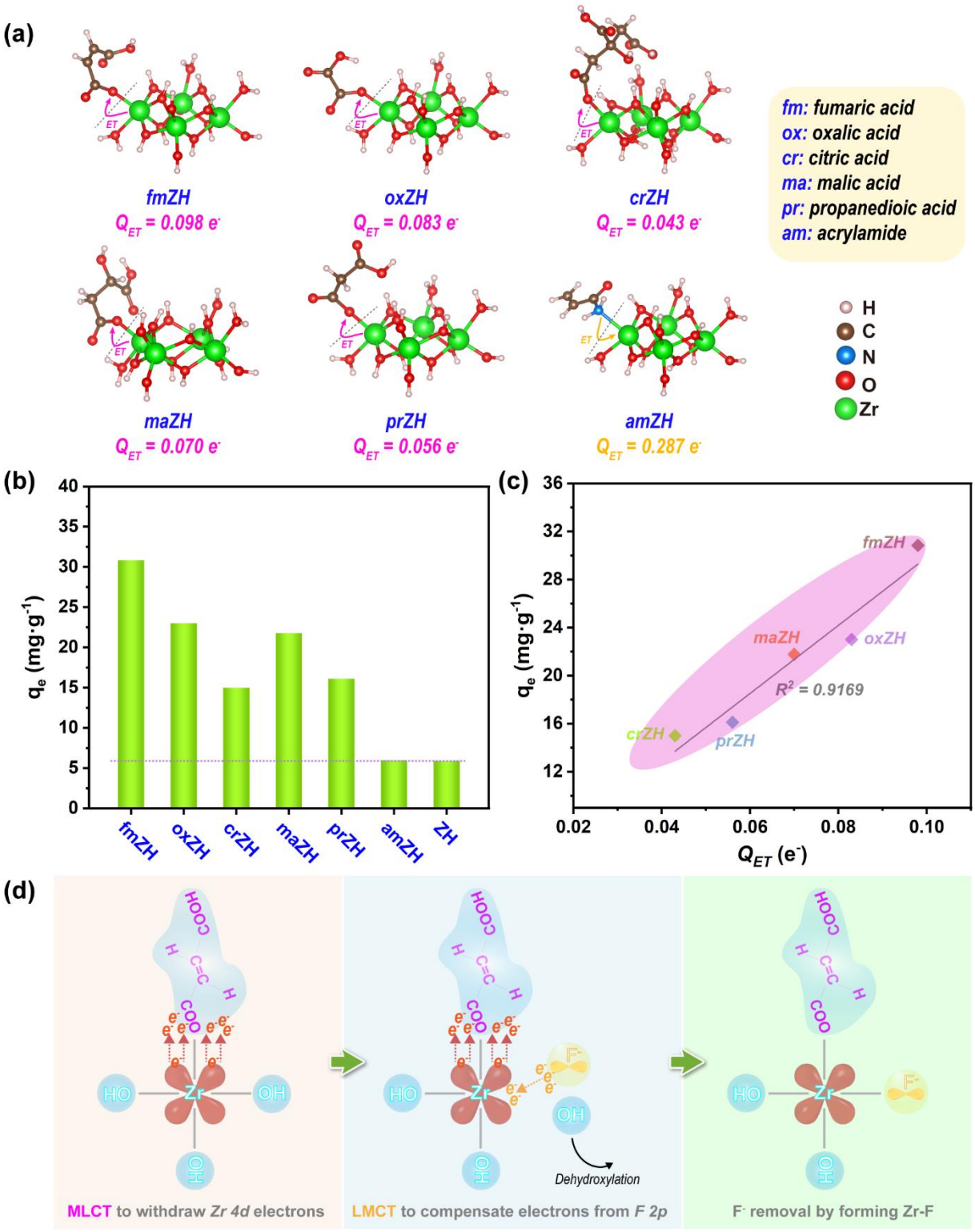

Figure 4. (**a**) Electron transfer between different ligands and Zr sites on ZH, (**b**) defluoridation capacity of ZH anchored by different ligands, (**c**) the relationship between electron transfer and defluoridation capacity, (**d**) schematic diagram of the mechanism of fluoride removal using fmZH.

The relationship between the adsorption capacity (q_e) and the quantity of transferred electrons (Q_{ET}) showed a positive linear correlation (R^2 = 0.9169) (**Figure 4c**), further confirming the key role of electron-withdrawing on the Zr site for enhanced defluoridation.

This could also confirm the result in the above analysis that the adsorption energy of fluorine ions was lower in the native Zr site than neighboring and opposite Zr sites (**Figure 3d**), probably because the electrons on native Zr site were more easily extracted by fumaric acid than neighboring and opposite Zr sites. Based on the above analysis, we proposed a schematic diagram of the mechanism of fluoride removal by fmZH (**Figure 4d**). Fumaric acid plays the role of an electron-withdrawing ligand, its carboxyl group and the Zr site on ZH undergo monodentate coordination to transfer electrons from Zr site to fumaric acid through the metal-to-ligand charge transfer (MLCT) process. The delocalized Zr sites increased the orbital energy level matching and vacated *Zr 4d* orbitals to promote hybridization with the *F 2p* orbitals of fluoride ions, ultimately the fluoride ion was removed by the ligand-to-metal charge transfer (LMCT) process to form stable Zr–F bond. The LMCT process can be demonstrated by the significant decrease in the Zr 3d binding energy (CHB@fmZH + F^-) (**Figure 3f**) and the negative electrostatic potential around Zr–F bond on the surface of fmZH (**Figure 3c**) after adsorption of fluoride ions, signifying that the missing electron density around the Zr site was compensated by adsorbed fluoride ions.

3. Conclusion

In this study, we applied template confinement-ligand anchoring strategy to obtain highly dispersed ultrafine fmZH (~3.4 nm) and achieve an adjustable electron density on its Zr sites. The saturation adsorption capacity and dynamic treatment capacity CHB@fmZH for fluoride ion were 10.8 times and 45.9 times higher than that of CHB@ZH, respectively. Defluoridation capacity was in positive linear relationship with the electron-withdrawing ability of ligands, including fumaric acid, oxalic acid, citric acid, malic acid and propanedioic acid. Especially, fumaric acid extracted 0.098 e^- from the Zr site on fmZH. Then electron delocalized Zr sites promoted the vacating of more *4d* orbitals of the Zr site to hybridize with the *2p* orbitals of the fluoride ion to form stable Zr–F bond for intensified defluoridation. This novel strategy of steering the electron density of Zr sites through ligand effect to enhance fluoride removal will

not only facilitate the mechanistic understanding of defluoridation, but also guide the design and synthesis of analogous adsorbents with high defluoridation efficiency.

4. Experimental Section

Materials and Reagents: Chitosan [$(C_6H_{11}NO_4)_n$, molecular weight: 700-800 kDa, deacetylation degree: ≥ 90%] was procured from Shanghai Lanji Biotechnology. Fumaric acid ($C_4H_4O_4$, AR) and $ZrOCl_2·8H_2O$ (99%, AR) were purchased from Shanghai Aladdin. Other reagents including NaOH, NaCl, $NaNO_3$, Na_2SO_4, $NaHCO_3$ and NaF were all analytically pure. All chemical reagents were not further purified. The deionized water (18.3 MΩ·cm) used in the experiments was obtained from Millipore ultra-pure water system.

Preparation of Fumaric Acid-Anchored Zirconium Hydroxide Confined Inside Chitosan Hydrogel Beads (CHB@fmZH): **Step 1:** 25.0 mmol $ZrOCl_2·8H_2O$ was dissolved in 100 mL of deionized water to obtain Zr^{4+} solution, then 2.0 g of chitosan was added and magnetically stirred for 12 h until the chitosan was completely dissolved to obtain chitosan-Zr^{4+} hydrosol. **Step 2:** the chitosan-Zr^{4+} hydrosol was poured into an acid burette (the inside diameter of the tip was 0.8 ~ 1.0 mm), and the hydrosol was added dropwise to the stirring NaOH solution (400 mL, 1.0 mol/L) by controlling the glass stopper, which was instantly solidified to form white hydrogel beads, followed by washing with deionized water to neutral to obtain zirconium hydroxide-chitosan hydrogel beads (abbreviated as CHB@ZH). **Step 3:** 31.0 mmol of fumaric acid (fm) was dissolved into 30 mL of 1.87 mol/L NaOH solution (the molar ratio of OH^- to fm was 1.81:1 to maintain the pH of fumarate solution at 3 ~ 4) to obtain fumaric acid solution under shaking, followed by the addition of 6 g CHB@ZH into this fumaric acid solution and then oscillatory reaction at room temperature for 24 h. Upon completion, the product was washed with deionized water for several times to neutral and stored in deionized water to finally obtain fumaric acid-anchored zirconium hydroxide confined inside chitosan hydrogel beads (CHB@fmZH). In addition, for comparison, CHB@fmZH with other contents of fumaric acid

(5.2, 10.3, 15.5, 20.7, or 41.4 mmol), chitosan hydrogel beads (CHB), chitosan hydrogel beads impregnated with fumaric acid (CHB@fm), and zirconium hydroxide (ZH) were prepared as detailed in **Text S1**, **Text S2** and **Text S3** in the **Supporting Information**. The structural parameters of all adsorbents were described in **Table S1** in **Supporting Information**.

Materials Characterization: The morphological structure of the materials was observed using a field emission ultra-high resolution scanning electron microscope (GeminiSEM 300, Zeiss, Germany) coupled with an EDS (Oxford X-MAX) for spot sweep analysis of the surface elements, and further observation with field emission transmission electron microscope (JEM-2100F, JEOL). To analyze the elemental distribution on the surface of the materials, a high-angle annular dark field-scanning transmission electron microscope (HAADF-STEM) coupled with a Bruker super-X EDS was used to perform a surface scan of the materials. X-ray diffraction (XRD) tests were performed using a powder X-ray diffractometer (AXS D8 Advance, Bruker) equipped with a Cu *Kα* radiation source (λ=1.5406Å) and a graphite monochromator to analyze the materials phase structure. The functional groups were analyzed using an infrared spectrometer (TENSOR II, Bruker, Germany). XPS spectra were recorded using X-ray photoelectron spectrometer (ESCALAB 250Xi, Thermo Scientific). N_2 adsorption-desorption measurements were performed on a Brunauer-Emmett-Teller surface area analyzer (ASAP 2020 HD88, Micromeritics, USA) to obtain the specific surface area values and pore structure information. Macropore information was further investigated using the fully automated mercury intrusion porosimetry (AutoPore V 9600, Micromeritics, USA). The zeta potentials on the surface of the materials in different pH solutions were determined using a zeta potential analyzer (Zetasizer ZEN 3600, Malvern).

Fluoride Ion Removal: Batch fluoride ion removal experiments were performed in 50 mL centrifuge tubes, and unless otherwise noted, ten beads of CHB@ZH (corresponding to total dry weight of 26.85 ± 0.94 mg) or CHB@fmZH (corresponding to total dry weight of 31.93 ± 1.38 mg) were added into 30 mL, 40 mg/L fluoride ion solution (pH = 7.0 ± 0.2) for all

adsorption tests. For the pH effect experiment, the pH range was adjusted from 3 to 12. In the adsorption isotherm experiment, the initial concentration of fluoride ion solution was adjusted to 10 ~ 310 mg/L. For the dose effect experiment, the number of beads was adjusted to 3 ~ 15, and the solid-liquid ratio was calculated using the wet mass. In the adsorption kinetics experiment, ten centrifuge tubes were prepared before the experiment, and the fluoride ion concentration was measured by taking out one centrifuge tube at intervals from 0 to 34 h until all tubes were removed. In the coexistence ion competition experiment, two gradients (0.01 and 0.1 mol/L) of Cl^-, NO_3^-, SO_4^{2-}, HCO_3^-, or $H_2PO_4^-$ were set for each competing ion. In the recycling experiments, CHB@fmZH after adsorption of fluoride ions was first shaken in 0.01 mol/L NaOH at room temperature for 12 h to dissociate adsorbed fluoride ions and washed with deionized water to neutral. Because the fumaric acid was shed from the surface of CHB@fmZH during desorption in NaOH solution, fumaric acid was used for regeneration after desorption (**Figure S12, Supporting Information**). Then cast into 31 mmol fumaric acid solution (solution volume 40 mL, pH = 3 ~ 4) for 24 h to complete the desorption-regeneration of fluoride-saturated sorbent. Dynamic fixed-bed column experiments were performed using a chromatographic column (inner diameter: 16 mm, length: 200 mm) filled with 5 mL of wet beads (CHB, CHB@ZH or CHB@fmZH). Water quality parameters for synthetic groundwater used in the column study were listed as follows: solution pH = 7.0 ± 0.2, F^- = 3.3 mg/L, K^+ = 39.0 mg/L, Na^+ = 115.0 mg/L, Ca^{2+} = 4.0 mg/L, Mg^{2+} = 2.4 mg/L, Cl^- = 213.0 mg/L, NO_3^- = 62.0 mg/L, SO_4^{2-} = 96.0 mg/L, and HCO_3^- = 61.0 mg/L. The synthetic groundwater was pumped into the chromatographic column using a constant-flow pump (BT100S, LEADFLUID, China) at a flow rate of 1.25 mL/min. The fluoride ion concentration was determined using a fluoride ion selective electrode (PXSJ-216F, Lei-ci, China). The concentration of fumaric acid in the experiment was determined by an ultra performance liquid chromatography (UPLC H-class, Waters, USA). The detector was an ultraviolet detector, the wavelength was 210 nm, the column was an ACQUITY UPLC® BEH C18 (2.1 × 100 mm, 1.7 μm) and the column

temperature was 40 °C. The injection volume was 10 μL, and the mobile phase was a mixture of 90% phosphoric acid (0.1%) and 10% methanol at a flow rate of 0.5 mL/min.

Supporting Information

Supporting Information is available from the Wiley Online Library or from the author.

Acknowledgements

This work was supported by the Basic Research Funds of the Central Public Welfare Research Institute (No. R-JBYWF-2021-D04, K-JBYWF-2021-ZT04, R-JBYWF-2021-D05), the National Natural Science Foundation of China (No. 22066022), the Natural Science Foundation of Science and Technology Bureau of Xi'an City (No. 21KJZZ0065), and the Tianjin Natural Science Foundation Project (No. 20JCYBJC00830). The main opinions and conclusions in this manuscript are those of the authors and should not be presented as opinions of the Ministry of Natural Resources of People's Republic of China.

Conflict of Interest

The authors declare no conflict of interest.

Data Availability Statement

The data that support the findings of this study are available in the supporting information of this article.

Received: ((will be filled in by the editorial staff))
Revised: ((will be filled in by the editorial staff))
Published online: ((will be filled in by the editorial staff))

References

[1] M. C. Smith, E. M. Lantz, H. V. Smith, *Science* **1931**, 74, 244.
[2] H. V. Churchill, *Ind. Eng. Chem.* **1931**, 23, 996.
[3] a) M. Barathi, A. S. K. Kumar, N. Rajesh, *Coord. Chem. Rev.* **2019**, 387, 121; b) S. Jagtap, M. K. Yenkie, N. Labhsetwar, S. Rayalu, *Chem. Rev.* **2012**, 112, 2454.
[4] a) J. Podgorski, M. Berg, *Nat. Commun.* **2022**, 13, 1; b) T. Yu, Y. Chen, Y. Zhang, X. Tan, T. Xie, B. Shao, X. Huang, *Chin. Chem. Lett.* **2021**, 32, 3410.
[5] R. H. McKee, *Ind. Eng. Chem.* **1934**, 26, 849.
[6] G. J. Fink, F. K. Lindsay, *Ind. Eng. Chem.* **1936**, 28, 947.
[7] a) A. C. Zettlemoyer, E. A. Zettlemoyer, W. C. Walker, *J. Am. Chem. Soc.* **1947**, 69, 1312; b) Q. Zhang, X. Tan, T. Yu, *Chin. Chem. Lett.* **2022**, DOI: 10.1016/j.cclet.2022.107748107748.
[8] A. E. Taylor, C. A. Jensen, *J. Am. Chem. Soc.* **1958**, 80, 5918.
[9] a) V. Sternitzke, R. Kaegi, J.-N. Audinot, E. Lewin, J. G. Hering, C. A. Johnson, *Environ. Sci. Technol.* **2012**, 46, 802; b) D. S. Mosiman, A. Sutrisno, R. Fu, B. J.

Marinas, *Environ. Sci. Technol.* **2021**, 55, 2639; c) H. Qiu, M. Ye, M.-D. Zhang, X. Zhang, Y. Zhao, J. Yu, *ACS ES&T Eng.* **2020**, 1, 46.
[10] P. L. T. Nur, T. C. Nguyen, S. Vigneswaran, J. K. G. Singh, *Chem. Eng. J.* **2014**, 247, 93.
[11] a) X. Dou, D. Mohan, C. U. Pittman, S. Yang, *Chem. Eng. J.* **2012**, 198-199, 236; b) D. Shen, Y. Song, X. Chen, Y. Zhou, H. Li, J. Pan, *Chem. Eng. J.* **2022**, 444, 136199; c) Q. Zhang, S. Bolisetty, Y. Cao, S. Handschin, J. Adamcik, Q. Peng, R. Mezzenga, *Angew. Chem. Int. Ed.* **2019**, 58, 6012; d) B. Pan, J. Xu, B. Wu, Z. Li, X. Liu, *Environ. Sci. Technol.* **2013**, 47, 9347; e) X. Zhang, L. Zhang, Z. Li, Z. Jiang, Q. Zheng, B. Lin, B. Pan, *Environ. Sci. Technol.* **2017**, 51, 13363; f) X.-p. Liao, B. Shi, *Environ. Sci. Technol.* **2005**, 39, 4628.
[12] a) C. Gao, X.-Y. Yu, T. Luo, Y. Jia, B. Sun, J.-H. Liu, X.-J. Huang, *J. Mater. Chem. A* **2014**, 2, 2119; b) C. Ren, M. Zhou, Z. Liu, L. Liang, X. Li, X. Lu, H. Wang, J. Ji, L. Peng, G. Hou, W. Li, *Environ. Sci. Technol.* **2021**, 55, 15082.
[13] a) C. R. N. Rao, J. Karthikeyan, *Water Air Soil Pollut.* **2012**, 223, 1101; b) E. Vences-Alvarez, L. H. Velazquez-Jimenez, L. F. Chazaro-Ruiz, P. E. Diaz-Flores, J. R. Rangel-Mendez, *J. Colloid Interface Sci.* **2015**, 455, 194.
[14] D. Kang, X. Yu, M. Ge, *Chem. Eng. J.* **2017**, 330, 36.
[15] a) X. Zhao, D. Liu, H. Huang, W. Zhang, Q. Yang, C. Zhong, *Microporous Mesoporous Mat.* **2014**, 185, 72; b) J. Su, M. Yuan, L. Han, H. Deng, J. Chang, Y. Zhuang, J. Wang, Y. Zhang, *Chem. Eng. J.* **2023**, 451, 138989.
[16] a) M. S. Mauter, I. Zucker, F. o. Perreault, J. R. Werber, J.-H. Kim, M. Elimelech, *Nat. Sustain.* **2018**, 1, 166; b) F. Pulizzi, W. Sun, *Nat. Nanotechnol.* **2018**, 13, 633; c) D. Jassby, T. Y. Cath, H. Buisson, *Nat. Nanotechnol.* **2018**, 13, 670.
[17] G. Shen, L. Pan, R. Zhang, S. Sun, F. Hou, X. Zhang, J. J. Zou, *Adv. Mater.* **2020**, 32, 1905988.
[18] Y. Jiang, Y.-P. Deng, R. Liang, N. Chen, G. King, A. Yu, Z. Chen, *J. Am. Chem. Soc.* **2022**, 144, 4783.
[19] C. Jian, W. Hong, Q. Cai, J. Li, W. Liu, *Appl. Catal. B-Environ.* **2020**, 266, 118649.
[20] Z. Fang, Z. Deng, A. Liu, X. Zhang, L. Lv, B. Pan, *J. Hazard. Mater.* **2021**, 414, 125505.
[21] a) B. L. Kirsch, S. H. Tolbert, *Adv. Funct. Mater.* **2003**, 13, 281; b) E. Aneggi, V. Rico-Perez, C. de Leitenburg, S. Maschio, L. Soler, J. Llorca, A. Trovarelli, *Angew. Chem. Int. Ed.* **2015**, 54, 14040.
[22] a) Y. Liao, W. Chen, S. Li, W. Jiao, Y. Si, J. Yu, B. Ding, *Small* **2021**, 17, e2101639; b) R. B. Balow, J. G. Lundin, G. C. Daniels, W. O. Gordon, M. McEntee, G. W. Peterson, J. H. Wynne, P. E. Pehrsson, *ACS Appl. Mater. Interfaces* **2017**, 9, 39747.
[23] a) K. D. Dobson, A. J. McQuillan, *Spectroc. Acta Pt. A-Molec. Biomolec. Spectr.* **1999**, 55, 1395; b) Y. S. Hwang, J. J. Lenhart, *Langmuir* **2008**, 24, 13934; c) A. Tran, G. Williams, S. Younus, N. N. Ali, S. L. Blair, S. A. Nizkorodov, H. A. Al-Abadleh, *Environ. Sci. Technol.* **2017**, 51, 9700.
[24] a) H. Ha, K. Shanmuganathan, C. J. Ellison, *ACS Appl. Mater. Interfaces* **2015**, 7, 6220−6229; b) P. Pleskunov, D. Nikitin, R. Tafiichuk, A. Shelemin, J. Hanus, I. Khalakhan, A. Choukourov, *J. Phys. Chem. B* **2018**, 122, 4187; c) K. L. M. Taaca, M. J. D. De Leon, K. Thumanu, H. Nakajima, N. Chanlek, E. I. Prieto, M. R. Vasquez, *Colloid Surf. A-Physicochem. Eng. Asp.* **2022**, 637, 128233.
[25] C. Zhang, X. Li, T. Li, M. Liu, K. Zhang, Y. Zheng, M. Lan, J. Zhang, Z. Zhang, *Anal. Chem.* **2021**, 93, 5145.
[26] T. W. Kim, S. Park, J. Oh, C.-H. Shin, Y.-W. Suh, *ChemCatChem* **2018**, 10, 3406.
[27] N. C. Abeykoon, S. F. Mahmood, S. B. Alahakoon, M. Wunch, R. A. Smaldone, D. J. Yang, J. P. Ferraris, *ACS Appl. Energy Mater.* **2021**, 4, 8988.

[28] a) B. Lin, M. Hua, Y. Zhang, W. Zhang, L. Lv, B. Pan, *Chemosphere* **2017**, 166, 422; b) X. Zhang, P. Huang, S. Zhu, M. Hua, B. Pan, *Environ. Sci. Technol.* **2019**, 53, 5319.